Available online at www.sciencedirect.com

ScienceDirect

Physics Procedia 83 (2016) 1435 – 1443

Physics Procedia

9th International Conference on Photonic Technologies - LANE 2016

Computational simulation of thermal and spattering phenomena and microstructure in selective laser melting of inconel 625

Tuğrul Özel[a,]*, Yiğit M. Arısoy[a], Luis E. Criales[a]

[a]*Manufacturing & Automation Research Laboratory, Department of Industrial and Systems Engineering, Rutgers University, New Jersey, USA*

Abstract

Computational modelling of Laser Powder Bed Fusion (L-PBF) processes such as Selective laser Melting (SLM) can reveal information that is hard to obtain or unobtainable by in-situ experimental measurements. A 3D thermal field that is not visible by the thermal camera can be obtained by solving the 3D heat transfer problem. Furthermore, microstructural modelling can be used to predict the quality and mechanical properties of the product. In this paper, a nonlinear 3D Finite Element Method based computational code is developed to simulate the SLM process with different process parameters such as laser power and scan velocity. The code is further improved by utilizing an in-situ thermal camera recording to predict spattering which is in turn included as a stochastic heat loss. Then, thermal gradients extracted from the simulations applied to predict growth directions in the resulting microstructure.

Peer-review under responsibility of the Bayerisches Laserzentrum GmbH

Keywords: Selective laser melting; Temperature; Spattering; Modelling

1. Introduction

Laser-based powder metal additive manufacturing technology has been steadily growing with applications in various industries for parts with complex geometries and structures (Kruth et al. 2007). Laser Powder Bed Fusion (L-PBF) processes such as Selective Laser Melting™, Direct Metal Laser Sintering™, and LaserCUSING™ in particular are advantageous in obtaining fully dense structures without a need for post processing unlike selective laser sintering (Yasa et al. 2011; Bourell et al. 2011) but requires higher energy levels and lower scan velocities. However, due to high energy densities applied with the laser beam and meltpool instabilities (Childs and Hauser

* Corresponding author. Tel.: +1-848-445-1099 ; fax: +1-848-445-5467 .
E-mail address: ozel@rutgers.edu

Peer-review under responsibility of the Bayerisches Laserzentrum GmbH
doi:10.1016/j.phpro.2016.08.149

2004), there remain some issues related to laser spattering and balling, material evaporation and keyhole effects (Simonelli et al. 2015). Resultant microstructure of the build part (Amato et al. 2012) and structural integrity is also a major concern (Brinksmeier et al. 2010) especially for nickel alloys Inconel 718 and Inconel 625 which are used in mission critical parts in aerospace applications.

In order to gain in-depth understanding of the Laser Powder Bed Fusion processing of nickel alloy 625 (Inconel 625), test coupons that were fabricated with different process conditions are analysed. An in-situ thermal camera video recording is performed and analysed for meltpool size, spattering particles and heating and cooling rates during processing of powder material. Furthermore, microstructure, grain size, and columnar grain growth directions are measured from scanning electron microscopy (SEM) images. Finite Element (FE) modeling is utilized to predict temperature gradients and directions in relation to columnar growth.

2. Experimental Approach

2.1. Laser powder bed fusion and experimental design

A commercial additive manufacturing grade (Micro-Melt 625AM) Inconel 625 powder produced by gas atomized process with the average particle size of 35μm from Carpenter company was used and solid coupons in the shape of cubes (16×16×15mm) were manufactured using an EOS M270 Direct Metal Laser Sintering (DMLS) machine under nitrogen gas ambience at the National Institute for Standards & Technology (NIST) facility located in Gaithersburg, Maryland, USA. The L-PBF system consisted of a single mode ytterbium fiber laser (IPG YLR-SM) with a maximum power of ~200 W and F-theta focusing objective that provides a variable spot size of ~100μm. In the experiments, 3-factor, 3-level Box-Behnken experimental design where low, medium and high settings of each factor are defined as P= 169, 182, 195 W, v_s= 725, 800, 875 mm/s, h=0.09, 0.10, 0.11 mm, for power (P), scan velocity (v_s), and hatch distance (h) respectively. Powder bed thickness is set at s=20 μm with about 55% powder packing density. Therefore, laser energy densities between 94.6 and 139.5 J/mm^3 into the powder bed was obtained as defined with Eq. 1.

$$E=P/(v_s \times h \times s) \tag{1}$$

The L-PBF process works by melting desired locations on the powder bed on a layer. The area to be processed is first divided into four stripes. Each stripe with 4 mm width consists of multiple tracks, separated by a hatch distance, and each track is processed with the laser beam at a constant scanning velocity. After a track is completed by the movement of laser in one direction, laser turns off about 0.042 ms and shifts towards the next unprocessed track and turns on again starting to move in the opposite direction of the previous track. Also two separate scan strategies (*SS*) with layer-to-layer counter clockwise rotation of 90° and ~67° angles are applied for obtaining uniformly dense built parts as shown in Fig. 1.

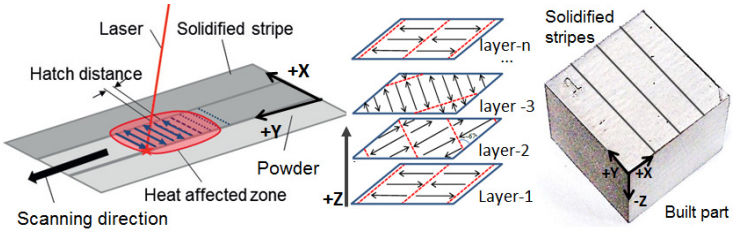

Fig. 1. Laser scanning of stripes with hatching and layer rotation in L-PBF.

The size of the molten region in the powder bed is determined by process parameters and powder material properties as well as process environmental effects. After a layer is finished, a new layer of powder, with a predefined thickness is placed on the powder bed. For a successful build, it is critical that the meltpool size is large

enough to connect tracks and stripes in each layer and deep enough to fuse with the previous layer. Inadequate or excessive process parameters can easily cause incomplete fusion or keyhole meltpool which leads to catastrophic failures during the process. Also, process parameters and layerwise scan strategy have a significant influence on the underlying microstructure of the part, which affects the resultant properties and fatigue life significantly [6].

2.2. Thermal measurements and spatter analysis

Thermal gradient measurement is highly important for various understanding of powder consolidation and solidification in L-PBF (Zaeh and Ott 2011; Krauss et al. 2014). In-situ monitoring of the process can be utilized to quantitatively analyze meltpool size and spattering phenomenon (Furumoto et al. 2013). For this purpose, an HFR thermal camera has been placed in the processing chamber door of the EOS DMLS machine and the process has been recorded for the nominal processing condition (P=195W, v_s=800mm/s, h=0.10mm, SSR=90°). The thermal camera has an integration time of 0.040 ms and can record at 1800 frames per second which translates into 0.5555 ms per frame. In the instantaneous field of view (iFoV), each pixel represents 36 μm and the camera is angled at 43.7° with ~150-mm distance. For the purpose of this study, it is important to note that for emittivity value of ε=0.2 used, only temperatures from 600 °C to 1380 °C can be very reliably calculated by the camera. Temperatures outside this range should be treated with caution. Three frames along a track (beginning, middle and end) from the thermal video recording are shown in Fig. 2.

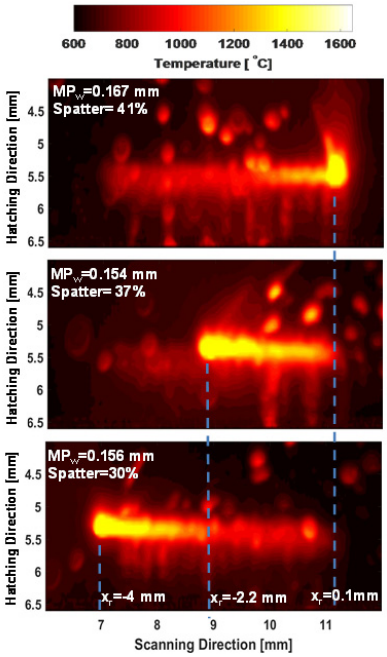

Fig. 2. Thermal image of powder surface during L-PBF processing (P=195 W, v_s=800mm/s, h=0.10mm, SS=90°).

To determine the size of meltpool from the thermal camera recording, each frame is processed individually such that pixels with temperatures exceeding the liquidus temperature (1350 °C for IN625) are segmented from colder pixels. During the processing of meltpool size calculations, it is observed that some of the laser spattering particles that are in close proximity to the meltpool affect the meltpool size calculation algorithm (Fig. 3).

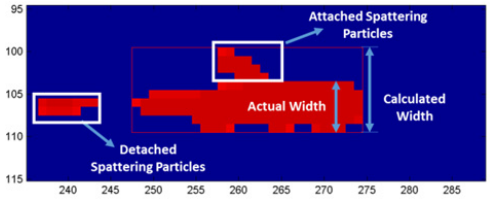

Fig. 3. Meltpool width measurements along with attached and detached spattering particles. (Dimensions are in pixels).

Measured melt pool width (MP_w), laser spatter (%S) at a location along a track (x_f) are shown in Fig. 2. A percentage of apparent spattering is calculated between 30-45% in the camera view area at different locations along the processed tracks. There exists some uncertainty. Firstly, the meltpool itself is very bright and spattering particles that occupy the same area as the meltpool in the frame are not recoverable from the images. Moreover, solidified regions are highly reflective, causing noise in the measurements. Furthermore, the recording angle of the camera as well as path and altitude of flying particles, combined with lens flares create an uncertainty in the data provided additional challenges. Lastly, camera calibration and measurement limitations exist for temperatures above 1150 °C combined with reflections from the surface of the processed area.

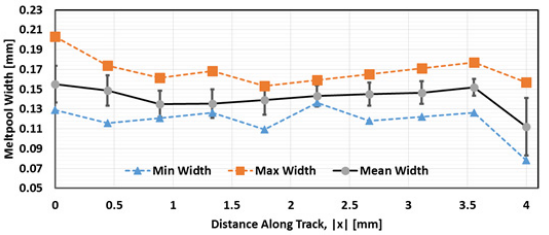

Fig. 4. Measured meltpool width along a single track in L-PBF of Inconel 625 as the mean, min and max width of 20 track measurements.

Fig. 4 shows the measured width of the meltpool as the mean of 20 tracks thermal camera images representing along the track length with 200 frames (10 frames per track). Minimum, maximum and mean temperatures observed at three different x locations: the beginning, middle and the end of the track, for the tracks with negative scanning directions are shown in Fig. 5. It is seen that the temperatures are very high at the beginning of the track when the processing starts, because the meltpool is located in this region. As the time passes, this point cools down. In contrast, the end of the track starts off with a low temperature, and heats up when the laser reaches and melts the region. As expected, the middle point of the track heats up as the laser approaches, and cools down as it departs. Average heating rate is around 600 °C/ms and cooling rate is about 150 °C/ms.

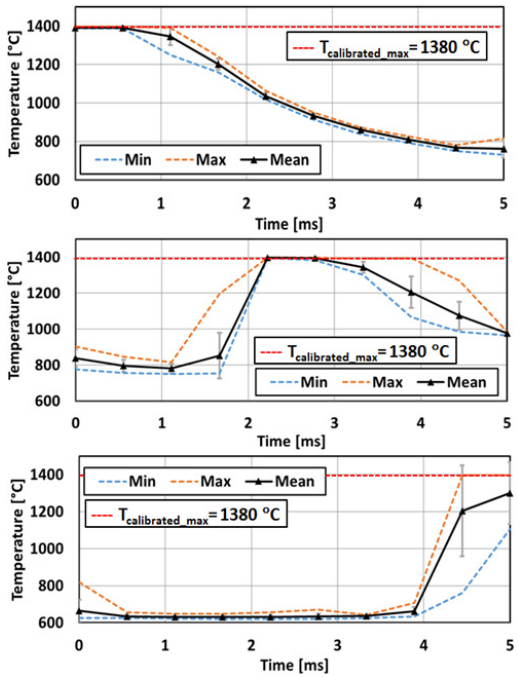

Fig. 5. Temperatures at the beginning of the track (top), middle of the track (middle) and end of the track (bottom) across multiple tracks.

2.3. Microstructure analysis

Due to the nature of the L-PBF process, processed layers are reheated many times during the processing of new layers, and the effect of reheating on the microstructure can only be observed from the interior layers. L-PBF machine processes the outer regions of the specimens with the so called “skin” parameters that are different than the user prescribed parameters. In order to analyse the microstructure of L-PBF processed Inconel 625 coupons, they are first ground to remove approximately 500 µm from the outside surfaces. After the grinding operation, the L-PBF coupons were electropolished about 50 µm to reveal the microstructure. Grain sizes and growth directions are indicative of cooling rates, and can affect the mechanical properties of the material significantly. SEM images were obtained from the prepared test coupons using the InLens and Secondary Electron (SE2) detectors, from XY, XZ and YZ surfaces at multiple locations and magnification levels. The images reveal a dendritic microstructure with cross sections of dendrites appearing as equiaxed grains (see Fig. 6). The dendrites appear to be growing in two main directions, in the build (*B*) direction and also in a direction perpendicular to the laser’s scanning path. During the processing, the scanning path changes many times, thus creating dendrites in different directions. The growth of dendrites in these two directions can be explained by temperature gradients as dendritic growth is observed when large gradients of temperature or concentration are present. In the case of L-PBF, the temperature gradient is largest in the build direction as the cooling occurs towards the base plate via conduction and towards the environment at the top layer dominantly via radiation (due to high temperatures) and to some extent convection (the chamber is not in vacuum).

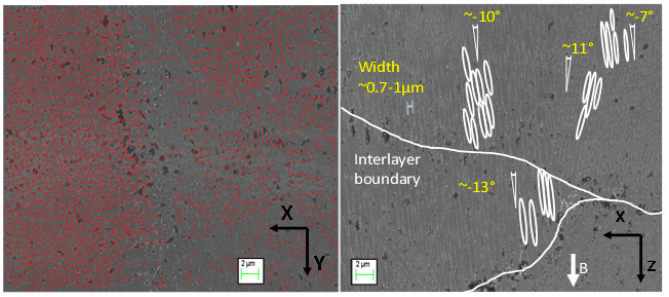

Fig. 6. SEM image of the electropolished XY surface of the Inconel 625 showing marked grains (left) and XZ surface showing columnar grains with inclinations (right). (P=195 W, v_s=800mm/s, h=0.10mm, SS=67°).

Fig. 6 shows the XZ surface of a coupon where columnar grains are observed in the build direction with approximately 0.75 µm in width. It is observed that the region between two curved meltpool boundaries contains equiaxed grains, whereas columnar grains as well as equiaxed grains are observed within the meltpool boundaries. An image processing procedure is applied on SEM images by marking grain boundaries in order to calculate the average diameters of the cellular grains commonly seen in the XY surface. In general, increasing the energy density causes an increase in the average grain sizes (see Fig. 7).

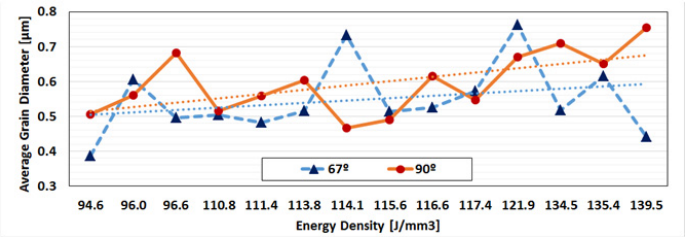

Fig. 7. Effect of energy density on the measured grain size on XY surface.

Laser power does not seem to affect the grain sizes significantly in both 67° and 90° rotation strategies. Increasing scanning velocity tends to decrease the grain sizes in both 67° and 90° rotation strategies. Increasing hatch distance tends to reduce the average grain diameters in the case of 90° rotation, whereas in the 67° rotation the change is not as significant. The effect of energy density on the measured growth direction angles is shown in **Fig. 8**. An overall decrease in magnitude is observed with increasing energy density in both positive and negative angles, suggesting that as the energy density increases, the grains tend to grow closer to the z (build) direction. However, the effect is highly nonlinear. Note that the 0° growth direction is considered positive in certain cases, and negative in some other cases. Since the bin sizes were 10°, each bin contained samples within the ±5° range of the bin center.

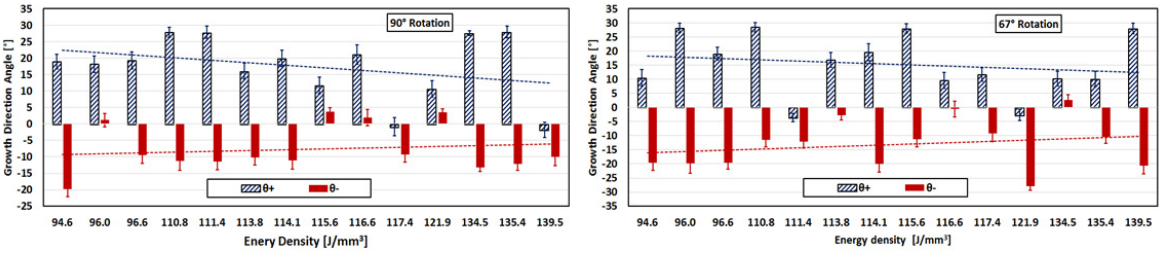

Fig. 8. Effect of energy density on the growth directions on XY surface.

3. Modeling and simulations

A nonlinear 3D Finite Element Method based MATLAB program is developed to simulate two-track L-PBF process at low (P= 169W, v_s=975 mm/s) medium (P=195W, v_s=800 mm/s), and high (P= 195W, v_s=725 mm/s) energy density settings of 134.5 J/mm^3, 121.9 J/mm^3, and 96.6 J/mm^3 respectively at a constant hatch distance of h=0.1 mm, and a layer thickness of s=20 μm (Arısoy 2016). The mesh geometry was 5 mm x 1 mm x 0.1 mm (5 layers). The bottom layer is assumed to be touching the base plate, which is kept at a constant temperature of 80°C (353 K). The mesh consists of 21450 isoparametric linear hexahedron elements, and is obtained with the Gmsh software. A Gaussian laser beam profile is implemented as a heat source and 3D diffusion equation is solved numerically. Temperature-dependent properties are employed (Table 1). The mesh is designed to allow an accurate representation of the laser beam; the smallest elements in the central region are 30μm×25μm×20μm in size which provided a sufficient resolution for the laser beam, while the largest elements are 30μm×100μm×20μm in size. The scanning starts on the top surface (z=0.1mm) at x=0.5mm, y=0.45mm, and the first track ends at x=0.5mm, y=4.6mm after 4.1 mm of scanning. At the end of the track, the laser is turned off for 0.042 ms. The laser then starts processing the second track beginning at x=4.6mm, y=0.55mm and ending at x=0.5mm, y=0.55 mm.

Table 1. Temperature-dependent material properties (Criales et al. 2016).

Liquidus Temperature, T_L [K]	1623
Solidus Temperature, T_S [K]	1563
Density, ρ [kg/m^3]	8440
Latent Heat of Fusion, L_f [kJ/kg]	227
Specific Heat, C_p [J/kg K] ($T \leq T_S$)	$338.98 + 0.2437 \times T$
Specific Heat, $C_{p,L}$ [J/kg K] ($T \geq T_L$)	735
Thermal conductivity, k [W/mK] ($T \leq T_S$)	$5.331 + 0.015 \times T$
Thermal conductivity, k [W/mK] ($T \geq T_L$)	30.05
Reflectivity, R	0.7

Predicted thermal field and measured thermal image are compared in Fig. 9. Meltpool widths extracted from the low, medium and high energy density FE simulation results are shown in Fig. 10. As expected, higher energy densities result in wider meltpools. Furthermore, Type-I meltpool (at the end of first track) and Type-II meltpool (at the beginning of second track) are observed for all cases at around 5 ms and 11 ms marks. The medium density FE simulation estimates the maximum meltpool width to be 130 μm, while the minimum meltpool width after reaching steady state is about 116 μm. Overall; the results are in good agreement with the measurements in Fig.4.

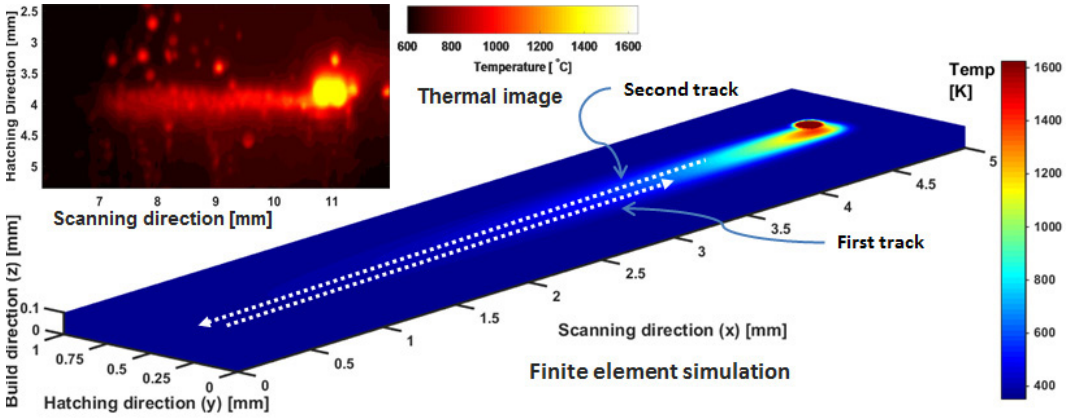

Fig. 9. Predicted thermal field and thermal image.

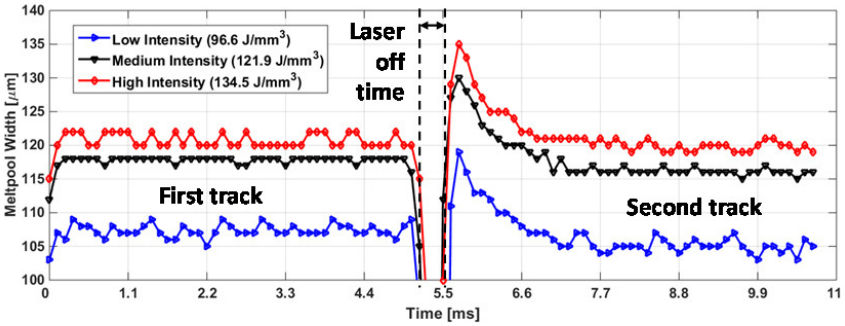

Fig. 10. Predicted melt pool sizes at three energy density settings.

The thermal gradients of the 3D FE solution from the YZ view at medium energy density of 121.9 J/mm^3 (see Fig. 11) depicts strong gradient vectors in the Z direction, caused by heating of the laser at the top and cooling of the base plate. The YZ view shows some heat diffusion in the Y direction, which indicate that the meltpool region also cools down towards the cooler regions on the sides of the track. This lateral cooling is further affected by the neighbouring material; solidified regions transfer the heat more effectively than powder regions. Other than the strong gradients in the Z direction in the XZ view, lateral cooling is also observed especially at the end of the track after x=4.5mm where the laser is turned off for a period of time (0.042ms) followed by the initiation of the scanning of the subsequent track, as the simulation models two tracks. These reveal the nature of solidification in L-PBF process as it is these thermal gradients that shape the microstructure during solidification.

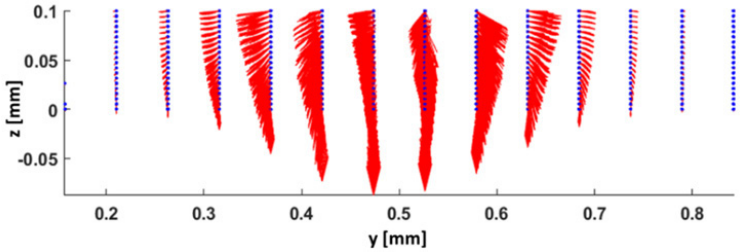

Fig. 11. Thermal gradients extracted from YZ view of FE solution.

At medium density, angles in XZ planes given in Fig. 12 show that majority of the heat diffusion aligns directly with the build direction, with a slight tilt towards the scanning direction indicated by the positive angles. The negative angles in XZ planes are in the opposite of the scanning direction, and result from the area near the beginning of the second track (x=4.6mm). It is observed that as the scanning velocity decreases, the 0° angles are tilted towards 10°, in the direction of scanning. Overall, these angles indicate the growth direction of columnar grains affected by the heat diffusion with respect to the build direction. It is noted that these angles largely coincide with the direction angles observed in Fig. 8.

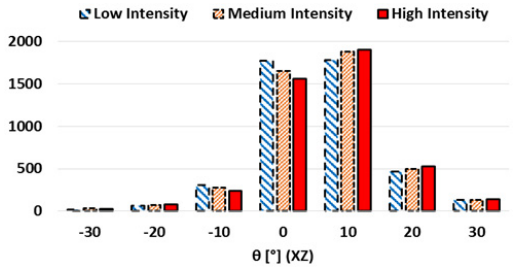

Fig. 12. Gradient directions in the XZ plane obtained from FE solutions.

4. Conclusions

This study provides investigations on resultant microstructure on the L-PBF built nickel alloy 625 test coupons. The relative density was found around 93.25%-99.25% Thermal measurements reveal Type-I meltpool size of 105µm-115µm and Type-II meltpool size of 135µm-155µm. The spatter was determined be 30-45% consisting of some vaporization. FE modeling provided 3D thermal field and thermal gradients with meltpool size predictions. The effects of process parameters and scan strategy rotation on the measured and predicted process variables that contribute to the growth direction of resultant columnar microstructure and overall built quality have been reported.

Acknowledgements

The support by the US-DOC NIST under the financial assistance number 70NANB14H227 and assistance by Dr. Shawn Moylan, Dr. Brandon Lane, and Dr. Alkan Donmez in designing and conducting experiments and acquiring in-situ thermal videos are gratefully acknowledged.

References

Amato KN, Gaytan SM, Murr LE, Martinez E, Shindo PW, Hernandez J, Collins S, Medina F, 2012. Microstructures and mechanical behavior of Inconel 718 fabricated by selective laser melting. *Acta Materialia* 60: 2229-2239.

Arısoy YM, 2016. *Physics-based simulation modeling and optimization of microstructural changes induced by machining and selective laser melting processes in titanium and nickel based alloys*. Ph.D. dissertation, Rutgers, The State University, New Brunswick, New Jersey, U.S.A.

Bourell DL, Leu MC, Chakravarthy K, Guo N, Alayavalli K, 2011. Graphite-based indirect laser sintered fuel cell bipolar plates containing carbon fiber additions. *CIRP Annals - Manufacturing Technology* 60(1): 275-278.

Brinksmeier E, Levy G, Meyer D, Spierings AB, 2010. Surface integrity of selective-laser-melted components. *CIRP Annals - Manufacturing Technology* 59 (1): 601-606.

Childs THC, Hauser C, Badrossamay M, 2004. Mapping and Modelling Single Scan Track Formation in Direct Metal Selective Laser Melting. *CIRP Annals - Manufacturing Technology* 53(1): 191-194.

Criales LE, Arısoy YM, Özel T, 2016. Sensitivity Analysis of Material and Process Parameters in Finite Element Modeling of Selective Laser Melting of Inconel 625. *International Journal of Advanced Manufacturing Technology*, DOI 10.1007/s00170-015-8329-y.

Furumoto F, Ueda T, Alkahari MR, Hosokawa A, 2013. Investigation of laser consolidation process for metal powder by two-color pyrometer and high-speed video camera. *CIRP Annals - Manufacturing Technology* 62(1): 223-226.

Krauss H, Zeugner T, Zaeh MF, 2014. Layerwise Monitoring of the Selective Laser Melting Process by Thermography. *Physics Procedia* 56: 64-71.

Kruth J-P, Levy G, Klocke F, Childs THC, 2007. Consolidation phenomena in laser and powder-bed based layered manufacturing. *CIRP Annals-Manufacturing Technology* 56(2): 730-759.

Simonelli M, Tuck C, Aboulkhair NT, Maskery I, Ashcroft I, Wildman RD, Hague R, 2015. A Study on the laser spatter and the oxidation reactions during Selective Laser Melting of 316L stainless steel, Al-Si10-Mg, and Ti-6Al-4V. *Metallurgical and Materials Transactions A* 46A: 3842-3851.

Yasa E, Kruth J-P, Deckers J, 2011. Manufacturing by combining Selective Laser Melting and Selective Laser Erosion/laser re-melting. *CIRP Annals- Manufacturing Technology* 60(1): 263-266.

Zaeh MF, Ott M, 2011. Investigations on heat regulation of additive manufacturing processes for metal structures. *CIRP Annals-Manufacturing Technology* 60(1): 259-262.